Mechanism and Constitutive Model of a Continuum Robot for Head Stabilization in Cancer Radiation Therapy.

Olalekan Ogunmolu†, Xinmin Liu⋆, Nicholas Gans‡, and Rodney D. Wiersma†

***Abstract*—We present a parallel robot mechanism and the constitutive laws that govern the deformation of its constituent soft actuators. Our ultimate goal is the real-time motion-correction of a patient's head deviation from a target pose where the soft actuators control the position of the patient's cranial region on a treatment machine. We describe the mechanism, derive the stress-strain constitutive laws for the individual actuators and the inverse kinematics that prescribes a given deformation, and then present simulation results that validate our mathematical formulation. Our results demonstrate deformations consistent with our radially symmetric displacement formulation under a finite elastic deformation framework.**

I. INTRODUCTION

Along with chemotherapy and surgery, radiation therapy (RT) is an effective cancer treatment modality, with more than half of all cancer patients managed by RT having higher survival rates [1]. This is in part due to the technological advancements that enable maximizing radiation dose to a tumor target, whilst simultaneously minimizing radiation to surrounding healthy tissues within a target volume.

To assure optimal dose delivery in RT, it is important for the patient to remain in a stable pose on the treatment machine. The current clinical convention for RT and stereotactic radiosurgery (SRS) is to immobilize the patient with rigid metallic frames or masks (see Figure 1). Frames attenuate the radiation dose (lowering treatment quality) owing to their metallic components, lack real-time motion compensation (hence the need for stopping the treatment when the patient deviates from a target position beyond a given threshold), and they cause patient discomfort and pain owing to their invasiveness [2]. The limitations of frames have spurred clinics using thermoplastic face masks. The masks decrease accuracy because of their flex which can cause a drift of up to 2-6mm; shrink and deformation in the mask's physical structure are also prominent arising from repeated use. Such motion correction precisions are not suitable for deep tumors located near critical structures such as the brain stem or for newer treatment modalities such as single isocenter multiple-target stereotactic radiosurgery (SRS), which are highly sensitive to rotational head motions.

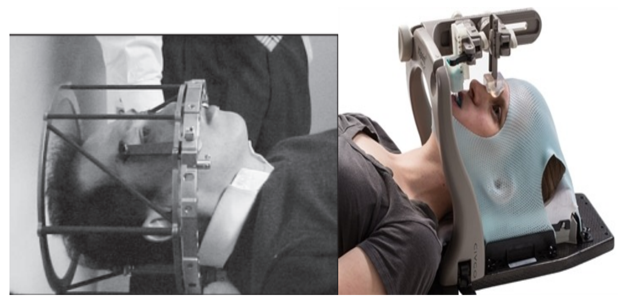

Fig. 1: *Left:* The Brown-Robert-Wells SRS Head Frame, reprinted from [3]. *Right:* Thermoplastic face mask. [Image best visualized in colored print].

To overcome these issues, explorative robotic positioning research studies have demonstrated the feasibility of maintaining stable patient cranial motion consistent with treatment plans platform [4]–[7]. For example, Belcher et al's Stewart-Gough platform [4] achieves ≤ 0.5mm and $\leq 0.5^\circ$ positioning accuracy 99% of the time. This system along with the plastic-based Ostyn et al's Stewart-Gough platform [8] use stepper motors to actuate the robot links. The 6-DOF robotic HexaPOD treatment couch of [7] was used in lung tumors treatment evaluation. Leveraging the fast and precise positioning of heavy payloads, the authors implemented a linear auto-regressive exogenous parameter-identification system to identify the HexaPOD's dynamics. [9] used an Elekta 4-DOF (3 translation and one rotational) parallel robot to first simulate and then control couch-based motion in real-time. The authors used a linear state-space model to approximate the rigid body dynamics of the patient support system earlier proposed in [10]. All these systems are accompanied by the following hazards:

- they share their dextrous workspace with the patients' body – a safety concern since these robots' rigid mechanical components are non-compliant;
- their lack of structural compliance mean that the patient experiences "hard shocks" when the end effector moves; and
- they are incapable of providing sophisticated motion compensation that may be needed for respiratory and internal organs displacement that often cause deviation from the target.
- their component electric motors and linear actuators suffer from the radiation attenuation problem and introduce

†Perelman School of Medicine, The University of Pennsylvania, Philadelphia, PA 19104, USA. {olalekan.ogunmolu, rodney.wiersma}@pennmedicine.upenn.edu
⋆Department of Radiation and Cellular Oncology, The University of Chicago, Chicago, IL 60637, USA. xmliu@uchicago.edu
‡Automation & Intelligent Systems Division, The University of Texas at Arlington Research Institute, Arlington, TX, USA. nick.gans@uta.edu
The research reported in this publication was supported by National Cancer Institute of the National Institutes of Health under award number R01CA227124.

serious safety concerns.

A. Contributions

This is why we have proposed inflatable air bladders (IABs) as motion compensators during F&M RT treatment (see [11]–[16]). In contrast to the stochastic system identification method used in deriving our earlier models, here, we regulate volume fractions within the IABs and spatial deformation based on specific mathematical relationships. Furthermore, we carve out a new class of IABs that are continuum, compliant, and configurable (C3) soft actuators that provide therapeutic patient head motion compensation. Contrary to remote-controlled airbags that have been used in upper mandible and head manipulation [17], our actuators deform based on their material moduli, compressed air pressurization and incompressibility constraints when given a reference trajectory. To our knowledge, ours are the first to explore C3 materials as actuation systems for cranial manipulation in robotic radiotherapy.

The constant curvature approach for parameterizing the deformation of continuum robots [18]–[20] has played a significant role in the kinematic synthesis of deformable continuum robots over the past three decades. Under this framework, the configuration space of a soft robot is parameterized by the curvature of an arc projected on its body, the arc's length, and the angle subtended by a tangent along that arc. The relationship between these parameters are typically found using differential kinematics with a Frenet-Serret frame that models a curve on the robot's surface with or without torsion. By abstracting an infinite dimensional structure to 3D, large portions of the manipulator dynamics are discarded under the assumption that the actuator design is symmetric and uniform in shape. This makes the constant curvature model overly simplistic so that it often exhibits poor performance in position control [21]. While the Cosserat brothers' beam theory has been relatively successful in modeling soft continuum dynamics [22], [23], its complexity, and sensing cost does not justify such alternatives [24]. Specifically, our **contributions** are as follows:

- We propose a minimally-invasive mechanism that largely avoids dose attenuation, whilst providing patient comfort during motion correction in F&M cancer RT;
- We derive a constitutive model for the robot's constituent actuators by extending the principles of nonlinear elastic deformations [25], [26] to strain deformations;
- We then analyze their deformation under stress, strain, internal pressurization, and an arbitrary hydrostatic pressure.

The rest of this paper is structured as follows: in § II, we present the overall C3 kinematic mechanism; we analyze the deformation properties of the IAB in § III; we then provide and discuss simulation results in § IV. We conclude the paper in § V.

II. Mechanism Synthesis

In our previous IAB models [14], we used a system identification approach to realize the overall system model. Our resultant model lumped the patient, treatment couch, as well as IAB models into one. The disadvantage of this approach was that such overall model lacked enough fidelity such that it necessitated the memory-based adaptive control composite laws that was derived from inverse Lyapunov analysis. Furthermore, the approximation model component of the ensuing neural-network controller required extensive training to realize a suitable controller for our head immobilization. Our goal here is to realize closed-form constitutive model for the IABs – capable of manipulating the complete patient's head DOF motion in real-time during RT.

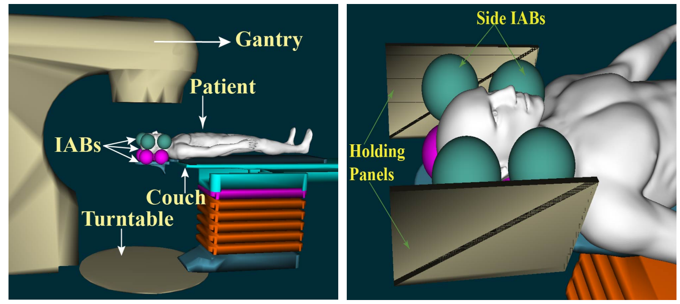

Fig. 2: **Left**. Gantry, Turntable, Patient and IABs around the patient's H&N Region (Panel removed for clarity). **Right**. Close-up setup view with holding PVC foam panels.

A. Type Synthesis

To design a mechanism that precisely manipulates a patient on a treatment table, optimizing the geometrical synthesis leaves many imponderables unresolved given the multitude of choices that arise, each calling for careful judgment in weighing advantages against disadvantages. Owing to the success of parallel mechanisms in precision manipulation tasks [27], we decide upon a profile-mechanism consisting of spherically-symmetric soft actuators arranged in a parallel manner around the patient's skull. We however recognize that other kinematicians may arrive at other linkage mechanisms that may offer better results. Our goal here is to find a high-fidelity model with tractable kinematics that can move the patient's head as desired on a treatment table.

B. Number Synthesis

We would like to have such freedom and constraint in the structural properties of our mechanism that enables rapid motion correction when a patient deviates from target. Prehensile control of the patient's cranial motion is attractive given its erstwhile success e.g. [17]'s airbag mechanism. In this sentiment, we choose eight IABs around the patient's head region as illustrated in Figure 2. The IABs are held in place around the head by low-temperature rigid PVC foam insulation sheet, encased in carbon fiber to prevent radiation beam attenuation. Velcro stickers (not shown) hold the IABs in place.

The freedoms provided by each IAB within the setup in Figure 2b are described as follows: the side actuators correct head motion along the *left-right* axis of the head anatomy including the yaw and roll motions, while the base IABs correct the head motion along the *anterior-posterior* axis [28, Ch. 2]. The *superior-inferior* motion is corrected by the two base actuators on the bottom of the neck. This arrangement offers

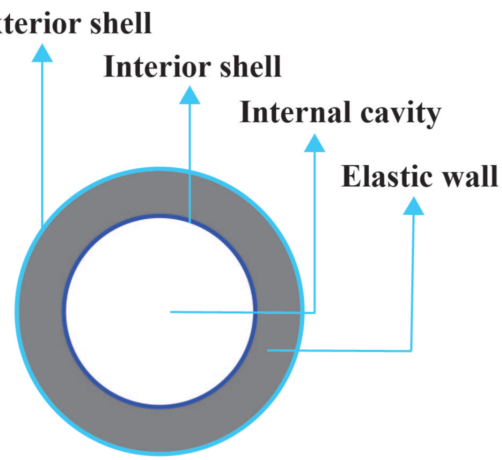

Fig. 3: Concentric circular shells around IAB's internal cavity.

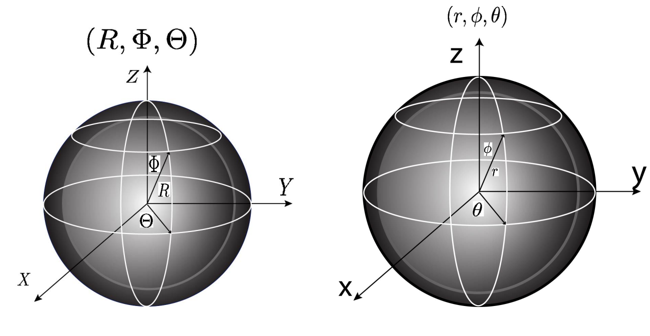

(a) Reference onfiguration *(b)* Current configuration

Fig. 4: IAB configurations in spherical polar coordinates.

prehensile manipulation via sensorless motion manipulation strategies within e.g. the vision-based sensor plan used in SRS or IMRT. By this, we mean the mechanical interactions of pushing or releasing by the IABs may be harnessed to further improve head manipulation robustness [29]–[31]. The IABs have an internal cavity which is surrounded by two elastic shells. The shells have radii $2.75 \pm 0.5cm$ and $3.0 \pm 0.5cm$ respectively and they have constant volume within their wall. The wall thickness is $0.25cm$, to accommodate flex and shrinking from repeated use as well as exhibit enough tensile strength that can move the patient's head whilst preserving its compliant properties. The geometry of an IAB is shown in Figure 3. The outer shell encapsulates the inner shell so that deformation follows a local volume preservation principle between configuration changes [25]. Deformation is achieved by supplying or removing compressed air from the internal IAB cavity. This fabrication procedure and hardware experiments will be described in a future publication.

III. Deformation Analysis of a Spherical IAB

In this section, we address the invariants, strains, and the constitutive stress laws that govern the deformation. We further derive the IAB kinematic equations. Our overarching assumption is that volume does not change locally during deformation at a configuration $\boldsymbol{\chi}(t)$ at time t. We work from a continuum mechanical hyperelastic approach, considering only final configurations for the soft robot; we thus drop the explicit dependence of a configuration on time and write it as $\boldsymbol{\chi}$. We refer readers to background reading materials in [25], [32] and [33]. We conclude this section by solving the boundary value problem under the assumption *incompressibility* of the IAB rubber material.

A. Deformation Invariants

For an elastic and incompressible IAB under the action of applied forces, the deformation is governed by a stored energy function, W, which captures the physical properties of the material [34]. We choose two invariants namely, I_1, and I_2, described in terms of the principal extension ratios, $\lambda_r, \lambda_\phi, \lambda_\theta$, of the IAB's strain ellipsoids. They are defined as

$$I_1 = \lambda_r^2 + \lambda_\phi^2 + \lambda_\theta^2, \quad \text{and} \quad I_2 = \lambda_r^{-2} + \lambda_\phi^{-2} + \lambda_\theta^{-2}. \tag{1}$$

Under the incompressibility assumptions of the IAB material, it follows that $\lambda_r \lambda_\phi \lambda_\theta = 1$ [26]. In spherical coordinates, the change in polar/azimuth angles as well as radii from the reference to current configurations are as illustrated in Figure 4. Forces that produce deformations are derived using the strain energy-invariants relationship, *i.e.* , $\frac{\partial W}{\partial I_1}$ and $\frac{\partial W}{\partial I_2}$.

B. Analysis of Strain Deformations

Suppose a particle on the IAB material surface in the reference configuration has coordinates (R, Φ, Θ) defined in spherical polar coordinates (see Figure 4), where R represents the radial distance of the particle from a fixed origin, Θ is the azimuth angle on a reference plane through the origin and orthogonal to the polar angle, Φ. Denote the internal and external radii as R_i and R_o respectively. We define the following constraints,

$$R_i \le R \le R_o, \quad 0 \le \Theta \le 2\pi, \quad 0 \le \Phi \le \pi. \tag{2}$$

Now, suppose that the IAB undergoes deformation upon pressurization of its internal cavity: arbitrary points A and A' in the reference configuration become Q and Q' in the current configuration. Let the *material element* (or fiber) vector that connects points A and A' be $a = a_R \boldsymbol{e}_r + a_\Theta \boldsymbol{e}_\Theta + a_\Phi \boldsymbol{e}_\Phi$, where $\boldsymbol{e}_R, \boldsymbol{e}_\Theta$, and $\boldsymbol{e}_\Phi$ are respectively the basis vectors for polar directions R, Θ, and Φ such that its axial length stretches *uniformly* by an amount $\lambda_z = \frac{r}{R}$.If spherical symmetry is maintained during deformation, we have the following constraints in the current configuration

$$r_i \le r \le r_o, \quad 0 \le \theta \le 2\pi, \quad 0 \le \phi \le \pi. \tag{3}$$

We define radial vectors $\mathbf{R}$ and $\mathbf{r}$ in spherical coordinates as,

$$\mathbf{R} = \begin{bmatrix} R \cos\Theta \sin\Phi, \\ R \sin\Theta \sin\Phi, \\ R \cos\Phi \end{bmatrix} \quad \text{and} \quad \mathbf{r} = \begin{bmatrix} r \cos\theta \sin\phi, \\ r \sin\theta \sin\phi, \\ r \cos\phi \end{bmatrix}. \tag{4}$$

The material volume $\frac{4}{3}\pi \left(R^3 - R_i^3\right)$ contained between spherical shells of radii R and R_i remains constant throughout deformation, being equal in volume to $\frac{4}{3}\pi\left(r^3 - r_i^3\right)$ so that

$$\frac{4}{3}\pi\left(R^3 - R_i^3\right) = \frac{4}{3}\pi\left(r^3 - r_i^3\right) \quad \text{or } r^3 = R^3 + r_i^3 - R_i^3. \tag{5}$$

The homogeneous deformation between the two configurations imply that

$$r^3 = R^3 + r_i^3 - R_i^3, \quad \theta = \Theta, \quad \phi = \Phi, \tag{6}$$

where the coordinates obey the constraints of equations (2) and (3). The Mooney-Rivlin strain energy for small deformations as a function of the strain invariants of (1), is,

$$W' = C_1(I_1 - 3) + C_2(I_2 - 3), \tag{7}$$

where C_1 and C_2 are appropriate choices for the IAB material moduli. The Mooney form (7) has been shown to be valid even for large elastic deformations, provided that the elastic materials exhibit incompressibility and are isotropic in their reference configurations [35]. For mathematical scaling purposes that will soon become apparent, we rewrite (7) as $W = \frac{1}{2}W'$ so that

$$W = \frac{1}{2}C_1(I_1 - 3) + \frac{1}{2}C_2(I_2 - 3). \tag{8}$$

The deformation gradient tensor in spherical-polar coordinates can be verified to be,

$$\begin{aligned} \mathbf{F} &= \lambda_r \boldsymbol{e}_r \otimes \boldsymbol{e}_R + \lambda_\phi \boldsymbol{e}_\phi \otimes \boldsymbol{e}_\Phi + \lambda_\theta \boldsymbol{e}_\theta \otimes \boldsymbol{e}_\Theta \\ &= \frac{R^2}{r^2}\boldsymbol{e}_r \otimes \boldsymbol{e}_R + \frac{r}{R}\boldsymbol{e}_\phi \otimes \boldsymbol{e}_\Phi + \frac{r}{R}\boldsymbol{e}_\theta \otimes \boldsymbol{e}_\Theta, \end{aligned} \tag{9}$$

where $\otimes$ denotes the dyadic tensor product. It can be verified that the radial stretch is $\lambda_r = \frac{R^2}{r^2}$. The principal stretches along the azimuthal and zenith axes imply that $\lambda_\theta = \lambda_\phi$. Since for an isochoric deformation, $\lambda_r \cdot \lambda_\theta \cdot \lambda_\phi = 1$, the principal extension ratios are

$$\lambda_r = \frac{R^2}{r^2}; \lambda_\theta = \lambda_\phi = \frac{r}{R}. \tag{10}$$

The invariant equations, in spherical-polar coordinates, are therefore a function of the right Cauchy-Green and finger deformation tensors [36] *i.e.* ,

$$I_1 = \mathbf{tr}(\mathbf{C}) = \frac{R^4}{r^4} + \frac{2\,r^2}{R^2}, \; I_2 = \mathbf{tr}\left(\mathbf{C}^{-1}\right) = \frac{r^4}{R^4} + \frac{2\,R^2}{r^2} \tag{11}$$

where, $\mathbf{C} = \mathbf{F}^T\mathbf{F}$ and $\mathbf{B} = \mathbf{F}\mathbf{F}^T$ are the right and left Cauchy-Green tensors respectively.

C. Stress Laws and Constitutive Equations

We are concerned with the magnitudes of the differential stress on the IAB skin from a mechanical point of view. **We do not rely on finite element methods in this work** but rather take the whole material as a single continuum structure with elastic properties. Since the IAB deforms at ambient temperature, we take thermodynamic properties such as temperature and entropy to have negligible contribution. The IAB material stress response, $\mathbf{G}$, at any point on the IAB's boundary at time t determines the Cauchy stress, $\boldsymbol{\sigma}$, as well as the history of the motion up to and at the time t [25]. The

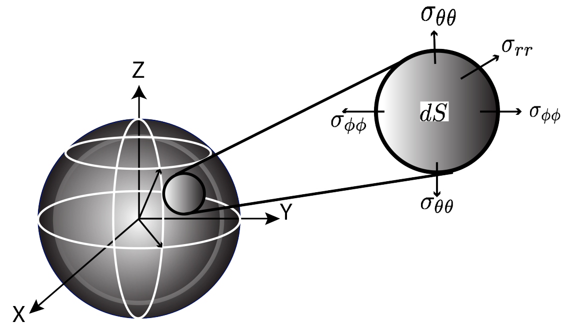

Fig. 5: Stress distribution on the IAB's differential surface, dS.

constitutive relation for the nominal stress deformation for an elastic IAB material is given by

$$\boldsymbol{\sigma} = \mathbf{G}(\mathbf{F}) + q\mathbf{F}\frac{\partial \boldsymbol{\Lambda}}{\partial \mathbf{F}}(\mathbf{F}), \tag{12}$$

where $\mathbf{G}$ is a functional with respect to the configuration $\boldsymbol{\chi}_t$, q acts as a Lagrange multiplier, and $\boldsymbol{\Lambda}$ denotes the internal (incompressibility) constraints of the IAB system. For an incompressible material, the indeterminate Lagrange multiplier becomes the hydrostatic pressure $i.e.$ $q = -p$ [32]. The incompressibility of the IAB material properties imply that $\boldsymbol{\Lambda} \equiv \det \mathbf{F} - 1$. Evaluating the partial derivative of $\boldsymbol{\Lambda}(\mathbf{F})$ with respect to $\mathbf{F}$ and substituting $-p$ for q in (12), we can verify that

$$\boldsymbol{\sigma} = \mathbf{G}(\mathbf{F}) - p\mathbf{I} \tag{13}$$

following the isochoric assumption $i.e.$, $\det(\mathbf{F}) = 1$. In terms of the stored strain energy, we find that

$$\boldsymbol{\sigma} = \frac{\partial W}{\partial \mathbf{F}}\mathbf{F}^T - p\mathbf{I} \tag{14}$$

where $\mathbf{I}$ is the identity tensor and p represents an arbitrary hydrostatic pressure. It follows that the constitutive law that governs the Cauchy stress tensor is

$$\begin{aligned} \boldsymbol{\sigma} &= \frac{\partial W}{\partial \mathrm{I}_1} \cdot \frac{\partial \mathrm{I}_1}{\partial \mathbf{F}}\mathbf{F}^T + \frac{\partial W}{\partial \mathrm{I}_2} \cdot \frac{\partial \mathrm{I}_2}{\partial \mathbf{F}}\mathbf{F}^T - p\mathbf{I} \\ &= \frac{1}{2}C_1\frac{\partial \mathbf{tr}\left(\mathbf{F}\mathbf{F}^T\right)}{\partial \mathbf{F}}\mathbf{F}^T + \frac{1}{2}C_2\frac{\partial \mathbf{tr}(\left[\mathbf{F}^T\,\mathbf{F}\right]^{-1})}{\partial \mathbf{F}}\mathbf{F}^T - p\,\mathbf{I} \\ &= \frac{1}{2}C_1\left(2.\mathbf{F}\mathbf{F}^T\right) + \frac{1}{2}C_2\left(-2\mathbf{F}(\mathbf{F}^T\,\mathbf{F})^{-2}\right)\mathbf{F}^T - p\,\mathbf{I} \\ &= C_1\mathbf{F}\mathbf{F}^T - C_2\left(\mathbf{F}^T\mathbf{F}\right)^{-1} - p\mathbf{I} \\ \boldsymbol{\sigma} &= C_1\mathbf{B} - C_2\mathbf{C}^{-1} - p\mathbf{I}, \end{aligned} \tag{15}$$

from which we can write the normal stress components as

$$\sigma_{rr} = -p + C_1\frac{R^4}{r^4} - C_2\frac{r^4}{R^4} \tag{16a}$$

$$\sigma_{\theta\theta} = \sigma_{\phi\phi} = -p + C_1\frac{r^2}{R^2} - C_2\frac{R^2}{r^2}. \tag{16b}$$

A visualization of the component stresses of (14) on the outer shells of the IAB material is illustrated in Figure 5.

D. IAB Boundary Value Problem

Here, we analyze the stress and internal pressure of the IAB at equilibrium. Consider the IAB with boundary conditions given by

$$\sigma_{rr}|_{R=R_o} = -P_{\text{atm}}, \quad \sigma_{rr}|_{R=R_i} = -P_{\text{atm}} - P \tag{17}$$

where P_{atm} is the atmospheric pressure and $P > 0$ is the internal pressure exerted on the walls of the IAB above P_{atm} *i.e.* , $P > P_{\text{atm}}$. Suppose that the IAB stress components satisfy hydrostatic equilibrium, the equilibrium equations for the body force $\boldsymbol{b}'s$ physical component vectors, b_r, b_θ, b_ϕ are

$$-b_r = \frac{1}{r^2}\frac{\partial r^2\sigma_{rr}}{\partial r} + \frac{1}{r\sin\phi}\frac{\partial \sin\phi\sigma_{r\phi}}{\partial\phi} + \frac{1}{r\sin\phi}\frac{\partial\sigma_{r\theta}}{\partial\theta} - \frac{1}{r}(\sigma_{\theta\theta} + \sigma_{\phi\phi}) \tag{18a}$$

$$-b_\phi = \frac{1}{r^3}\frac{\partial r^3\sigma_{r\phi}}{\partial r} + \frac{1}{r\sin\phi}\frac{\partial \sin\phi\sigma_{\phi\phi}}{\partial\phi} + \frac{1}{r\sin\phi}\frac{\partial\sigma_{\theta\phi}}{\partial\theta} - \frac{\cot\phi}{r}(\sigma_{\theta\theta}) \tag{18b}$$

$$-b_\theta = \frac{1}{r^3}\frac{\partial r^3\sigma_{\theta r}}{\partial r} + \frac{1}{r\sin^2\phi}\frac{\partial \sin^2\phi\sigma_{\theta\phi}}{\partial\phi} + \frac{1}{r\sin\phi}\frac{\partial\sigma_{\theta\theta}}{\partial\theta} \tag{18c}$$

(see [37]). From the equation of balance of linear momentum (*Cauchy's first law of motion*), we have that

$$\text{div } \boldsymbol{\sigma}^T + \rho\mathbf{b} = \rho\dot{\mathbf{v}} \tag{19}$$

where ρ is the IAB body mass density, div is the divergence operator, and $\mathbf{v}(\mathbf{x}, t) = \dot{\boldsymbol{\chi}}_t(\boldsymbol{X})$ is the velocity gradient. Owing to the incompressibility assumption, we remark in passing that the mass density is uniform throughout the body of the IAB material. When the IAB is at rest, $\dot{\mathbf{v}}_t(\mathbf{x}) = 0 \,\forall\, \mathbf{x} \in \mathcal{B}$ such that equation (19) loses its dependence on time. The assumed regularity of the IAB in the reference configuration thus leads to the steady state conditions for Cauchy's first equation; the stress field $\boldsymbol{\sigma}$ becomes *self-equilibrated* by virtue of the spatial divergence and the symmetric properties of the stress tensor, so that we have

$$\mathbf{div}\ \boldsymbol{\sigma} = 0. \tag{20}$$

Equation 20 is satisfied if the hydrostatic pressure p in (15) is independent of θ and ϕ. Therefore, we are left with (18a) so that we have

$$\frac{1}{r}\frac{\partial}{\partial r}(r^2\sigma_{rr}) = (\sigma_{\theta\theta} + \sigma_{\phi\phi}). \tag{21}$$

Expanding, we find that

$$\frac{1}{r}\left[r^2\frac{\partial\sigma_{rr}}{\partial r} + \sigma_{rr}\frac{\partial(r^2)}{\partial r}\right] = (\sigma_{\theta\theta} + \sigma_{\phi\phi})$$

$$r\frac{\partial\sigma_{rr}}{\partial r} = \sigma_{\theta\theta} + \sigma_{\phi\phi} - 2\sigma_{rr} \tag{22}$$

$$\frac{\partial\sigma_{rr}}{\partial r} = \frac{1}{r}(\sigma_{\theta\theta} + \sigma_{\phi\phi} - 2\sigma_{rr}). \tag{23}$$

Integrating the above equation in the variable r, and taking $\sigma_{rr}(r_\circ) = 0$, we find that

$$\begin{aligned}\sigma_{rr}(r) &= -\int_{r_i}^{r_\circ}\frac{1}{r}(\sigma_{\theta\theta} + \sigma_{\phi\phi} - 2\sigma_{rr})dr, \\ &= -\int_{r_i}^{r_\circ}\left[2C_1\left(\frac{r}{R^2} - \frac{R^4}{r^5}\right) + 2C_2\left(\frac{r^3}{R^4} - \frac{R^2}{r^3}\right)\right]dr.\end{aligned} \tag{24}$$

The above relation gives the radial stress in the current configuration. Suppose we are in the current configuration and we desire to revert to the reference configuration, we may carry out a change of variables from r to R as follows,

$$\begin{aligned}\sigma_{rr}(R) &= -\int_{R_i}^{R_\circ}\frac{1}{r}(\sigma_{\theta\theta} + \sigma_{\phi\phi} - 2\sigma_{rr})\frac{dr}{dR}dR, \\ &= -\int_{R_i}^{R_\circ}\left[2C_1\left(\frac{1}{r} - \frac{R^6}{r^7}\right) - 2C_2\left(\frac{R^4}{r^5} - \frac{r}{R^2}\right)\right]dR.\end{aligned} \tag{25}$$

In the same vein, using the boundary condition of $(17)|_2$ and taking the ambient pressure $P_{\text{atm}} = 0$, we find that the internal pressure $P = -\sigma_{rr}(r)$ *i.e.*

$$\begin{aligned}P(r) &= \int_{r_i}^{r_\circ}\left[2C_1\left(\frac{r}{R^2} - \frac{R^4}{r^5}\right) + 2C_2\left(\frac{r^3}{R^4} - \frac{R^2}{r^3}\right)\right]dr \\ P(R) &\equiv \int_{R_i}^{R_\circ}\left[2C_1\left(\frac{1}{r} - \frac{R^6}{r^7}\right) - 2C_2\left(\frac{R^4}{r^5} - \frac{r}{R^2}\right)\right]dR.\end{aligned} \tag{26}$$

Equations (25) and (26) completely determine the inverse kinematics of the IAB material: given a desired expansion or compression of the IAB walls, it calculates the internal pressurization or stress tensor necessary to achieve such deformation. Under the incompressibility of the IAB material properties we have,

$$r^3 = R^3 + r_i^3 - R_i^3, \text{ and } {r_\circ}^3 = R_\circ^3 + r_i^3 - R_i^3. \tag{27}$$

IV. Simulation Results

We conduct simulations under volumetric deformation with different shell properties (stated in the tables of Figure 6 and 7). We fix both reference configuration radii and choose realistic volumetric moduli for the IAB shells (with C_1 being the material's Young's modulus and C_2 its stiffness). By specifying a desired radially symmetric expansion for the inner IAB material, we test the local volume preservation property of (5) and evaluate the resulting displacement of the outer IAB skin, by applying the computed pressure (by virtue of (26)) between configurations.

We used the partial differential equations toolbox in Matlab in creating multispheres that correspond to the size synthesis described in § II-B and in solving the integrands of (25) and (26). The computed soft mesh model of the IAB is shown in the top left of the charts while the stress distribution after the application of the calculated pressure (by virtue of (26)) is shown in the top-right of the figures. We chose a Poisson's ratio of ≈ 0.45 (since the material shells are made of incompressible rubber materials) and a uniform mass density set at $0.1kg/m^3$ for the IAB (owing to its volume preserving property). The

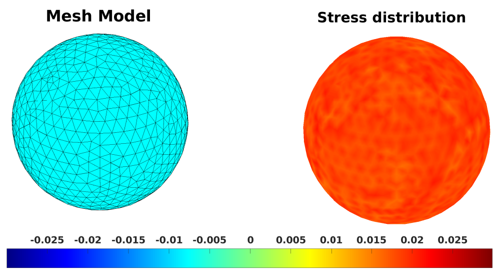

(a) **Left**: Mesh model. **Right**: Stress distribution on outer skin.

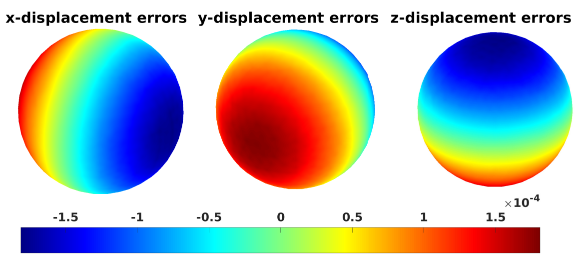

(b) Displacement errors along sphere's rectangular Cartesian coordinates.

Inputs					Outputs		
C_1	C_2	R_i	r_i	$R_\circ$	$r_\circ$	P	ΔV
$1.1e4$	$2.2e4$	$.027$	$.03$	$.03$	$.033$	$.76$	$\approxeq 0$

Fig. 6: Volumetric Deformation (Expansion).

radii dimensions are in m, the pressure is given in Pascals unless otherwise stated, C_1 and C_2 are appropriate material moduli, and ΔV is the volumetric change between the IAB shells between configurations (given in m^3).

A. Volumetric Expansion

In Figure 6 we test finite elastic deformation of the IAB material shells. The internal and external radii in the reference configuration are $.027m$ and $.03m$ and the task here is to to achieve a volumetric expansion so that in the current configuration, the internal radius is $.03m$. By (6), we found $r_\circ$ to be $.033m$. The stress distribution on the skins of the IAB is uniformly distributed based on the single value of the stress in every region of the surface; this signifies an equal amount of stress exertion on the walls of the actuator to achieve a desired deformation. This is confirmed in the bottom part of Figure 6 where we notice a displacement error of $0.15mm$, precise enough for prehensile motion manipulation of the head as we would require in the enumerated applications for this soft actuator model.

B. Volumetric Compression

Figure 7 depicts the volumetric compression of the incompressible IAB under the application of the derived internal pressure. For a desired uniform displacement $0.002m$, our results confirm the validity of the stress-strain constitutive laws, as we again notice a displacement error of $\approxeq 10^{-4}m$ along the sphere's Cartesian axes in the lower charts of Figure 7. The negative pressure in the table signify that air is being drawn out of the IAB. Again, our results show consistency with respect to local volume preservation and radially symmetric displacement.

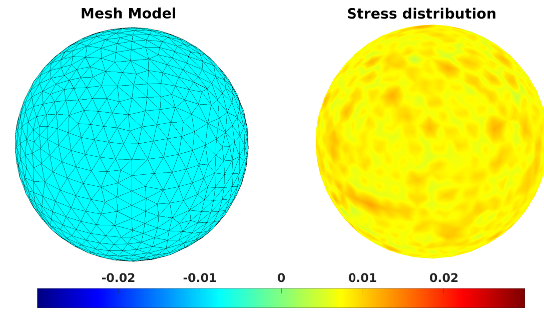

(a) **Left**: Mesh model. **Right**: Stress distribution on outer skin.

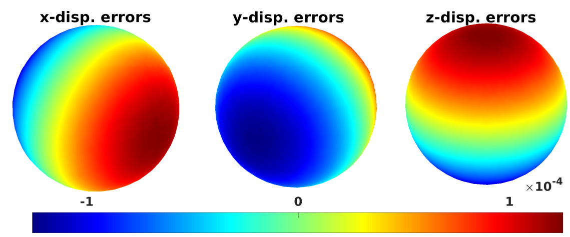

(b) Displacement errors along sphere's rectangular Cartesian coordinates.

Inputs					Outputs		
C_1	C_2	R_i	r_i	$R_\circ$	$r_\circ$	P	ΔV
$1.1e4$	$2.2e4$	$.025$	$.03$	$.03$	$.028$	$-.3385$	$\approxeq 0$

Fig. 7: Volumetric Deformation (Compression).

V. Conclusions

We have presented a patient's head motion-correction mechanism and the constitutive laws that governs the deformation of its constituent soft actuators. The derived model was tested with spheres with size small enough to accommodate a head on a treatment table as shown in Figure 2. Our results confirm the fidelity of this model given its high accuracy in precise displacements. In future work, we will integrate a time element into the soft inverse kinematics relation to accommodate the physical system; this is essential because the compressed air source needs to be shut off from supplying or removing air from the IAB cavities once a desired radius is achieved.

VI. Acknowledgments

A vote of thanks to Professor Raymond W. Ogden of The University of Glasgow and Audrey Sedal of The University of Michigan for their feedback on the constitutive model discussed in this work.

References

[1] L. Gaspar *et al.*, "Recursive Partitioning Analysis (rpa) of Prognostic Factors in three Radiation Therapy Oncology Group (rtog) Brain Metastases Trials," *Int. J. Radiat. Oncol. Biol. Phys.*, vol. 37, p. 745751, 1997. 1

[2] T. Takakura, T. Mizowaki, M. Nakata, S. Yano, T. Fujimoto, Y. Miyabe, M. Nakamura, and M. Hiraoka, “The geometric accuracy of frameless stereotactic radiosurgery using a 6d robotic couch system,” *Physics in Medicine & Biology*, vol. 55, no. 1, p. 1, 2009. 1

[3] R. Chelvarajah, B. Leighton, L. Martin, W. Smith, and R. Beldham-Collins, “Cranial immobilisationis there a better way?” *Radiographer*, vol. 51, no. 1, pp. 29–33, 2004. 1

[4] A. Belcher, “Patient Motion Management with 6-DOF Robotics for Frameless and Maskless Stereotactic Radiosurgery,” Ph.D. dissertation, The University of Chicago, 2017. 1

[5] X. Liu, A. H. Belcher, Z. Grelewicz, and R. D. Wiersma, “Robotic stage for head motion correction in stereotactic radiosurgery,” in *2015 American Control Conference (ACC)*. IEEE, 2015, pp. 5776–5781. 1

[6] X. Liu and R. D. Wiersma, “Optimization based trajectory planning for real-time 6DoF robotic patient motion compensation systems,” *PloS one*, vol. 14, no. 1, p. e0210385, 2019. 1

[7] C. Herrmann, L. Ma, and K. Schilling, “Model Predictive Control For Tumor Motion Compensation In Robot Assisted Radiotherapy,” *IFAC Proceedings Volumes*, vol. 44, no. 1, pp. 5968–5973, 2011. 1

[8] M. Ostyn, T. Dwyer, M. Miller, P. King, R. Sacks, R. Cruikshank, M. Rosario, D. Martinez, S. Kim, and W.-H. Yeo, “An Electromechanical, Patient Positioning System For Head And Neck Radiotherapy,” *Physics in Medicine & Biology*, vol. 62, no. 18, p. 7520, 2017. 1

[9] O. C. Haas, P. Skworcow, D. Paluszczyszyn, A. Sahih, M. Ruta, and J. A. Mills, “Couch-Based Motion Compensation: Modelling, Simulation and Real-time Experiments,” *Physics in Medicine & Biology*, vol. 57, no. 18, p. 5787, 2012. 1

[10] O. Haas, G. Bueno, R. Spriestersbach, H. Himmler, K. Burnham, and J. Mills, “Imaging And Control For Adaptive Radiotherapy,” *IFAC Proceedings Volumes*, vol. 38, no. 1, pp. 25–30, 2005. 1

[11] O. Ogunmolu, N. Gans, S. Jiang, and X. Gu, “An Image-Guided Soft Robotic Patient Positioning System for Maskless Head And Neck Cancer Radiotherapy: A Proof of Concept Study,” *Medical Physics: The International Journal of Medical Physics Research and Practice, Presented at the AAPM Meeting, Anaheim, CA*, vol. 42, pp. 3266–3266, June 2015. 2

[12] O. P. Ogunmolu, X. Gu, S. Jiang, and N. R. Gans, “A Real-Time, Soft Robotic Patient Positioning System for Maskless Head and Neck Cancer Radiotherapy: An Initial Investigation,” in *Automation Science and Engineering (CASE), 2015 IEEE International Conference on, Gothenburg, Sweden*. IEEE, 2015, pp. 1539–1545. 2

[13] O. P. Ogunmolu, X. Gu, S. Jiang, and N. R. Gans, “Vision-based Control of a Soft Robot for Maskless Head and Neck Cancer Radiotherapy,” in *Automation Science and Engineering (CASE), 2016 IEEE International Conference on, Fort Worth, Texas*. IEEE, 2016, pp. 180–187. 2

[14] O. Ogunmolu, A. Kulkarni, Y. Tadesse, X. Gu, S. Jiang, and N. Gans, “Soft-NeuroAdapt: A 3-DOF Neuro-Adaptive Patient Pose Correction System for Frameless and Maskless Cancer Radiotherapy,” in *IEEE/RSJ International Conference on Intelligent Robots and Systems (IROS), Vancouver, BC, CA*. IEEE, 2017, pp. 3661–3668. 2

[15] O. P. Ogunmolu, “A Multi-DOF Soft Robot Mechanism for Patient Motion Correction and Beam Orientation Selection in Cancer Radiation Therapy.” Ph.D. dissertation, The University of Texas at Dallas; UT Southwestern Medical Center, 2019. 2

[16] O. Ogunmolu and R. D. Wiersma, *Towards Real-Time Motion Compensation in Radio-Transparent Robotic Radiation Therapy.* 2

[17] S. Ishizaka, S. Moromugi, M. Kobayashi, H. Kajihara, K. Koga, H. Sugahara, T. Ishimatsu, S. Kurata, J. P. Kirkness, K. Oi, *et al.*, “A remote-controlled airbag device can improve upper airway collapsibility by producing head elevation with jaw closure in normal subjects under propofol anesthesia,” *IEEE journal of translational engineering in health and medicine*, vol. 2, pp. 1–9, 2014. 2

[18] M. W. Hannan and I. D. Walker, “Kinematics and the Implementation of an Elephant’s Trunk Manipulator and Other Continuum Style Robots,” *Journal of Robotic Systems*, vol. 20, no. 2, pp. 45–63, 2003. 2

[19] M. W. Hannan and I. D. Walker, “Novel Kinematics for Continuum Robots.” Advances in Robot Kinematics, 2000, pp. 227–238. 2

[20] B. A. Jones and I. D. Walker, “Kinematics for Multisection Continuum Robots.pdf,” vol. 22, no. 1, pp. 43–55, 2006. 2

[21] A. D. Kapadia, K. E. Fry, and I. D. Walker, “Empirical investigation of closed-loop control of extensible continuum manipulators,” in *2014 IEEE/RSJ International Conference on Intelligent Robots and Systems*. IEEE, 2014, pp. 329–335. 2

[22] F. Renda, M. Giorelli, M. Calisti, M. Cianchetti, and C. Laschi, “Dynamic model of a multibending soft robot arm driven by cables,” *IEEE Transactions on Robotics*, vol. 30, no. 5, pp. 1109–1122, 2014. 2

[23] D. Trivedi, A. Lotfi, and C. D. Rahn, “Geometrically Exact Models For Soft Robotic Manipulators,” *IEEE Transactions on Robotics*, vol. 24, no. 4, pp. 773–780, 2008. 2

[24] T. George Thuruthel, Y. Ansari, E. Falotico, and C. Laschi, “Control Strategies for Soft Robotic Manipulators: A Survey,” *Soft Robotics*, vol. 5, no. 2, pp. 149–163, 2018. 2

[25] R. Ogden, *Non-linear Elastic Deformations*. Mineola, New York: Dover Publicationbs, Inc., 1997. 2, 3, 4

[26] L. R. G. Treloar, *The physics of rubber elasticity*. Oxford University Press, USA, 1975. 2, 3

[27] J. Merlet, *Parallel robots*. Springer, 2015. 2

[28] K. H. Hunt, *Kinematic Geometry of Mechanisms*. Oxford University Press, 1977. 2

[29] J. F. Canny and K. Y. Goldberg, “”risc” industrial robotics: recent results and open problems,” in *Proceedings of the 1994 IEEE international conference on robotics and automation*. IEEE, 1994, pp. 1951–1958. 3

[30] M. A. Erdmann and M. T. Mason, “An exploration of sensorless manipulation,” *IEEE Journal on Robotics and Automation*, vol. 4, no. 4, pp. 369–379, 1988. 3

[31] M. T. Mason, *Mechanics of robotic manipulation*. MIT press, 2001. 3

[32] G. A. Holzapfel, T. C. Gasser, and R. W. Ogden, “A new constitutive framework for arterial wall mechanics and a comparative study of material models,” *Journal of elasticity and the physical science of solids*, vol. 61, no. 1-3, pp. 1–48, 2000. 3, 4

[33] A. Gent, *Engineering with Rubber. How to Design Rubber Components*. Munich: Carl Hanser Verlag Publicationbs, 2012. 3

[34] R. S. Rivlin and D. W. Saunders, “Large Elastic Deformations of Isotropic Materials. VII. Experiments on the Deformation of Rubber,” *Philosophical Transactions of the Royal Society A: Mathematical, Physical and Engineering Sciences*, vol. 243, no. 865, pp. 251–288, 1950. 3

[35] M. Mooney, “A theory of large elastic deformation,” *Journal of applied physics*, vol. 11, no. 9, pp. 582–592, 1940. 4

[36] A. Kaye, R. Stepto, W. Work, J. Aleman, and A. Y. Malkin, “Definition of terms relating to the non-ultimate mechanical properties of polymers (recommendations 1998),” *Pure and applied chemistry*, vol. 70, no. 3, pp. 701–754, 1998. 4

[37] Y. Fung, P. Tong, and X. Chen, *Classical and computational solid mechanics*. World Scientific Publishing Company, 2001, vol. 2. 5